C-end rule peptide-guided niosomes for prostate cancer cell targeting

Nicola d'Avanzo [a,1], Valeria Sidorenko [b,1], Lorena Simón-Gracia [b], Antonella Rocchi [b,c], Ilaria Ottonelli [d,e], Barbara Ruozi [e], Francesca Longo [b,c], Christian Celia [c,f,g,*], Tambet Teesalu [b,h,**]

[a] Department of Clinical and Experimental Medicine, University of Catanzaro "Magna Græcia", Viale "S. Venuta" s.n.c., Catanzaro I-88100, Italy
[b] Laboratory of Precision and Nanomedicine, Institute of Biomedicine and Translational Medicine, University of Tartu, Ravila 14b, 50411 Tartu, Estonia
[c] Department of Pharmacy, University of Chieti – Pescara "G. d'Annunzio", Via dei Vestini 31, Chieti I-66100, Italy
[d] Clinical and Experimental Medicine PhD Program, University of Modena and Reggio Emilia, 41125 Modena, Italy
[e] Nanotech Lab, Te.Far.T.I., Department of Life Sciences, University of Modena and Reggio Emilia, 41125 Modena, Italy
[f] Laboratory of Drug Targets Histopathology, Institute of Cardiology, Lithuanian University of Health Sciences, A. Mickeviciaus g. 9, Kaunas LT-44307, Lithuania
[g] Institute of Nanochemistry and Nanobiology, School of Environmental and Chemical Engineering, Shanghai University, Shanghai 200444, China
[h] Materials Research Laboratory, University of California, Santa Barbara, CA 93106, United States

ARTICLE INFO

ABSTRACT

The use of nanoformulations in drug delivery has a significant impact to increase the drug therapeutic efficacy and improve their safety in anticancer treatments. Non-ionic surfactant vesicles (NSVs), or niosomes, are a class of nanocarriers that are low-cost, physiochemical stable, and represent a promising alternative to liposomes. Tumor-penetrating C-end Rule (CendR) peptides, that target neuropilin-1 (NRP-1), a cell surface receptor commonly overexpressed on solid tumor cells, are widely used for precise delivery of diagnostic and therapeutic nanoparticles to malignant lesions. In this study, we investigated the impact of NSV functionalization with prototypic CendR peptide RPARPAR (abbr. RPAR) on NRP-1-dependent targeting of prostate cancer cells. Doxorubicin (DOX)-loaded NSVs, with or without RPAR conjugation, were prepared, physicochemical characterized, and finally tested for NRP-1 binding in human primary prostate carcinoma-1 and prostate carcinoma epithelial cell lines (PPC-1 and 22Rv1, respectively) that are NRP-1 positive, and melanoma (M21) cells that are NRP-1 negative. We demonstrated that the cellular uptake of RPAR-NSVs was NRP-1-dependent and the uptake rate of RPAR-NSVs was ca. ten times higher than un-targeted NSVs in PPC-1 cells; while no significant differences, between targeted and un-targeted nanocarriers, were obtained in M21 cell line. These data were further confirmed by using NRP-1 CendR-binding pocket-blocking (mAb7E8) antibody, which significantly inhibited the internalization of RPAR-NSVs in PPC-1 cells from ca. 80%–3%. The resulting data obtained of cytotoxic studies agreed the uptake results, thus showing a significant increase of cytotoxic effect for RPAR-NSVs@DOX in PPC-1 and 22Rv1 cells compared to NSVs@DOX. These results provide a proof of concept that the conjugation of CendR peptides on the surface of NSVs can increase the specific targeting of nanoparticles in NRP-1 positive cells, thus improving the therapeutic efficacy of resulting targeted nanocarriers for cancer treatment. Our results have important implications for the development of more efficient and selective cancer therapies and support further *in vivo* studies by using more complex targeting peptides, such as iRGD or other CendR peptides, that are also targeting primary recruitment receptors (i.e. integrins) and are then proteolytically activated into CendR peptides in the tumor microenvironment.

* Corresponding author. Department of Pharmacy, University of Chieti – Pescara "G. d'Annunzio", Via dei Vestini 31, Chieti I-66100, Italy.
** Corresponding author. Laboratory of Precision and Nanomedicine, Institute of Biomedicine and Translational Medicine, University of Tartu, Ravila 14b, 50411 Tartu, Estonia.
E-mail addresses: c.celia@unich.it (C. Celia), tambet.teesalu@ut.ee (T. Teesalu).
[1] These authors contributed equally.

1. Introduction

Prostate cancer has claimed more than 375,000 lives worldwide in 2020, and despite the improved therapy efficacy, it remains the fifth major cause of male death worldwide, with approximately 1.4 million new cases reported annually [1,2]. Age, family history, genetic mutations, and lifestyle factors such as obesity, smoking, and diet are the primary risk factors associated with prostate cancer incidence, progression, and recurrence [3–5]. Radical prostatectomy is often the first-line treatment for this disease and is typically combined with hormonal therapies due to the strong correlation between androgenic hormones and prostate cancer relapse. However, sometimes prostate cancer becomes resistant to these therapies, necessitating adjuvant chemotherapy [6]. Unfortunately, conventional chemotherapies have several drawbacks, including the emergence of drug resistance, mismatched pharmacokinetic profiles between individual chemotherapy regimens, and dose-limiting toxicities in normal organs. These disadvantages reduce the efficacy of chemotherapies and lead to side effects that compromise patients' compliance [7]. The use of nanocarriers as drug delivery systems (DDSs) has emerged as one possible solution to improve the efficacy and selectivity of anticancer therapeutics and reduce drug-induced resistance [8–11].

Numerous nanocarriers, such as liposomes, polymeric nanoparticles, and protein-based nanoparticles, have been studied for their potential applications in prostate cancer therapy [12–16]. Non-ionic surfactant vesicles (NSVs), also known as niosomes, have emerged as a promising alternative to liposomes. Whereas the bilayer structure and supramolecular architecture of NSVs is similar to liposomes, NSVs have higher physicochemical stability and lower manufacturing costs [17,18]. Like liposomes, the surface of NSVs can be readily modified with biomolecules and targeting ligands, such as peptides, proteins, and antibodies, to selectively target specific cells in the tumor microenvironment. This targeted approach can improve the effectiveness of drug payloads and minimize off-target effects [19,20].

Tumor-penetrating peptides (TPPs) are a specialized class of affinity-targeting peptides that home to tumor lesions, extravasate, and penetrate deep into the tumor parenchyma [21]. Upon initial accumulation in tumor blood vessels, TPPs activate an endocytic transport pathway related to macropinocytosis through a three-step process. This process involves binding to a primary tumor-specific endothelially-expressed receptor, proteolytic cleavage, and binding to a second receptor, NRP-1, which activates the transport pathway [22]. The prototypic tumor-penetrating peptide iRGD (clinically developed as Cend-1 and LSTA-1) is currently undergoing phase II clinical testing in pancreatic cancer patients [23,24]. The tissue-penetrating ability of iRGD and other tumor-penetrating peptides depends critically on the engagement of proteolytically activated C-end Rule (CendR) peptidic motif with NRP-1 receptors overexpressed in tumors on the surface of malignant and stromal cells [25]. All tumor-penetrating peptides share a crucial element, the cryptic R/KXXR/K motif, which can only interact with the C-terminal exposed cell and tissue penetration receptor NRP-1 upon proteolytic activation [25]. The CendR receptor NRP-1 plays a crucial role in angiogenesis, as well as in the regulation of vascular and blood-brain barrier permeability and CendR peptide-displaying ligands are involved in interactions of viral particles with NRP-1-expressing cells [26]. NRP-1 is overexpressed in malignant and malignancy-associated cells in solid tumors such as malignant melanomas, lung cancer, prostate cancer and in leukemia [27,28]. The targeting of NRP-1 with the prototypic CendR peptide RPAR represents a simple and robust system that can be used to optimize the delivery of homing peptide-guided nanoparticles [29].

In this study, we developed CendR-guided NSVs and established their ability to specifically engage with NRP-1 positive prostate cancer cells *in vitro*. We also showed that RPAR-NSVs loaded with the commonly used anthracycline drug doxorubicin (DOX) exhibit NRP-1-dependent toxicity towards cultured prostate carcinoma cells. These proof-of-concept studies support the feasibility of CendR-targeted NSV-based delivery platform.

2. Materials and methods

2.1. Materials

Cholesterol (Chol) and Tween 20 (Tw20) were obtained from Acros Organics (Acros Organics BVBA, Geel, Belgium), while 1,2-distearoyl-*sn*-glycero-3-phosphoethanolamine-N-[maleimide (polyethylene glycol)-2000] (ammonium salt) (DSPE-PEG2000-mal) was purchased from Avanti Polar (Suffolk, UK). Doxorubicin hydrochloride was provided by Carbosynth Ltd (Compton Berkshire, United Kingdom). FAM-Cys-Ahx-RPARPAR-OH (FAM-Cys-RPAR, FAM = c arboxyfluorescein, Ahx = aminohexanoic acid) and FAM-Cys-(Ahx)-RRAAPRP-OH (scrambled peptide or scrRPAR), were purchased from TAG Copenhagen, Denmark. Amicon Ultra 0.5 mL centrifugal filters with a nominal cut-off of 100 kDa were purchased from Millipore, Sigma, US. Paraformaldehyde (PFA) and human plasma were obtained from Sigma-Aldrich, Germany. Dulbecco's Modified Eagle Medium (DMEM) and phosphate-buffered saline (PBS) pH 7.4 were purchased from Lonza, Belgium. Trypan Blue was purchased from Gibco (Thermo Fischer Scientific, USA). Bovine serum albumin (BSA) and fetal bovine serum (FBS) were purchased from Capricorn Scientific, Germany. 3-(4,5-dimethylthiazol-2-yl)-2,5-diphenyltetrazolium bromide reagent (MTT) was purchased from Sigma Aldrich, Germany. PPC-1 human primary prostate cancer cells and M21 human melanoma cells were kindly provided by Erkki Ruoslahti laboratory at Research Center Sanford Burnham Prebys Medical Discovery Institute and by prof. David Cheresh at University of California San Diego (USA), respectively. All other reagents and chemicals used during the study were of analytical grade and were used without further purification.

2.2. Methods

2.2.1. Synthesis of RPAR-NSVs

NSVs were synthesized by using thin layer evaporation method as previously reported with some changes [30]. After hydration and extrusion, RPAR or scrRPAR were conjugated to the surface of resulting niosomes through the reaction between thiol group in the backbone of peptide and maleimide residual on the nanovesicles surface [31]. When required DOX was loaded into nanocarriers by remote loading procedure [30]. Before further investigations, nanovesicles were purified in order to remove no-entrapped DOX and unreacted peptides.

Details of the synthesis of RPAR-NSVs are reported in the Supplementary data.

2.2.2. Physicochemical characterization of NSVs

The Average size, polydispersity index (PDI), and zeta-potential of NSVs were measured with a Zetasizer Ultra (Malvern Instruments Ltd, Malvern, UK). After dilution in Hepes buffer solution or water samples were analyzed at 25 °C as previously reported [32]. The Nanoparticle tracking analysis (NTA) was carried out using a ZetaView PMX 120 V4.1 instrument (Particle Metrix GmbH, Ammersee, Bavaria, Germany) as previously reported [33] and compared to dynamic light scattering (DLS) analysis. The average diameter and the shape of nanocarriers were further studied by using the Transmission Electron Microscopy (TEM) analysis, as previously described with some modification [34].

The amount of RPAR conjugated to NSVs was quantified by measuring the fluorescence of 5-carboxyfluorescein (5-FAM) group included in the peptide's backbone structure [35].

The successful conjugation of RPAR peptide to DSPE-PEG2000-maleimide was further studied by ^{1}H NMR analysis [36].

The physical stability over time of RPAR-NSVs@DOX and NSVs@DOX (control) were studied by using Turbiscan Lab analysis as previously described [37] and by DLS analysis up to 4 weeks after
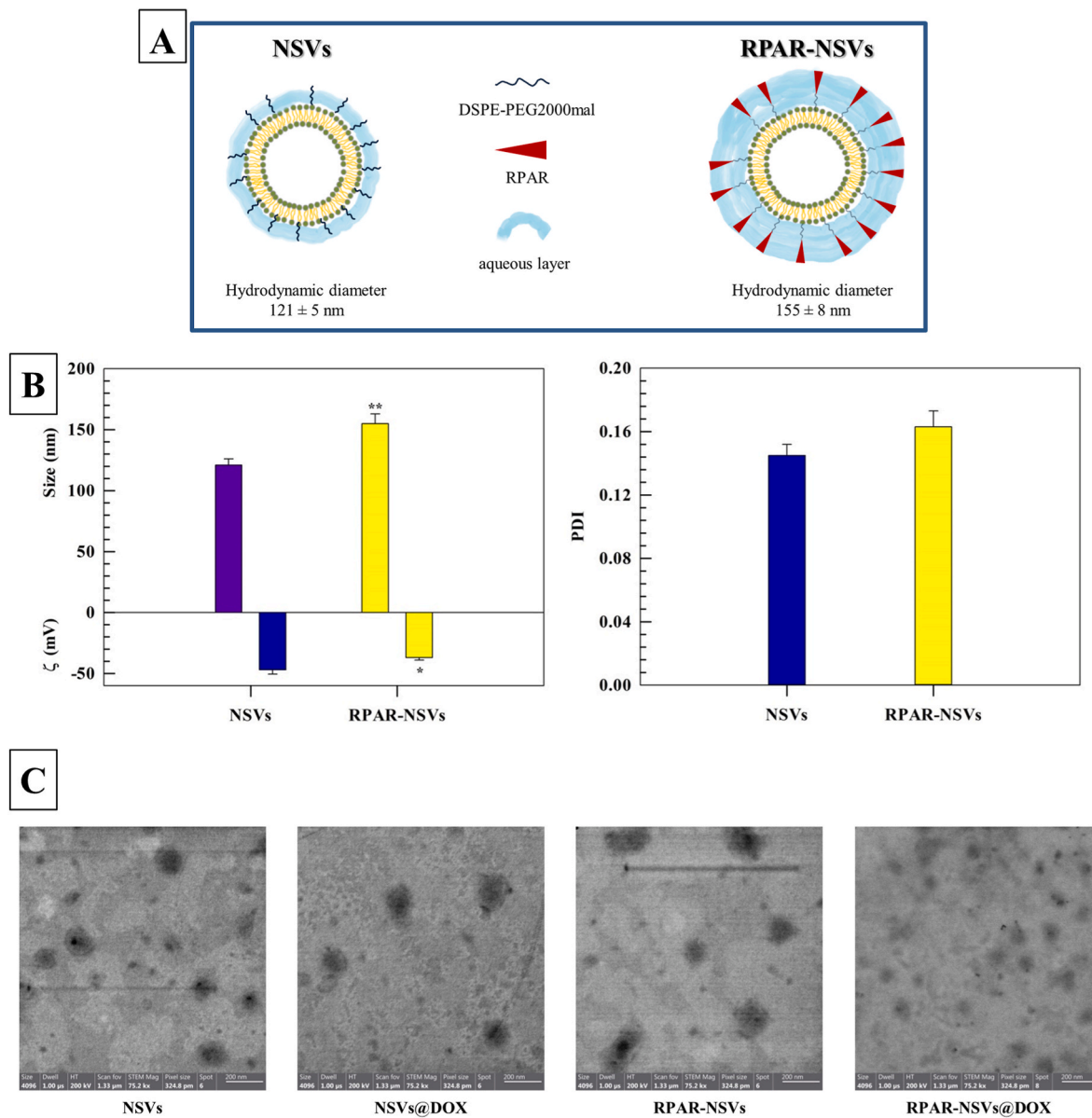
Fig. 1. Physicochemical characterization of NSVs. Panel A depicts a schematic representation of the increased aqueous layer surrounding the surface of NSVs after RPAR conjugation. Panel B shows the main physicochemical properties of the NSVs and RPAR-NSVs, including the average size, zeta potential (ζ), and polydispersity index (PDI), while features of DOX-loaded nanosystems are reported in the supplementary materials (Table S1). Panel C showed transmission electron microscopy (TEM) photograms; scale bar (200 nm) is embedded in each photogram and was automatically acquired during analysis. The results presented are the average of three independent experiments ± standard deviation. Statistically significant differences are shown as: *p < 0.05 and **p < 0.01 (NSVs vs RPAR-NSVs).

suitable storage of nanocarriers at +4 °C.

Details of the physicochemical characterization of RPAR-NSVs are reported in the Supplementary data.

2.2.3. Cell free binding studies

The cell-free binding study was carried out by coating Ni-NTA magnetic agarose beads (Qiagen GmbH, Hilden, Germany) with histidine-tagged recombinant b1b2 domain of NRP-1 or mutant NRP-1 b1b2 (containing mutated CendR-binding pocket) as previously reported [38].

Details of cell free binding studies are reported in the Supplementary data.

2.2.4. DOX entrapment efficiency and kinetic release profiles

The amount of DOX entrapped inside NSVs and released from RPAR-NSVs@DOX and NSVs@DOX was calculated according to Equations (1)

and (2), respectively.

$$E.E.\% = \frac{D_{en}}{D_{tot}} \times 100 \tag{1}$$

where, D_{en} corresponds to the amount of encapsulated drug while D_{tot} is the total amount of drug added during the NSVs synthesis.

$$\textbf{Drug released } \% = \left(\frac{drug_{rel}}{drug_{load}} * \textbf{d.f.} \right) \times 100 \tag{2}$$

where, $drug_{rel}$ is the amount of drug released at a selected time point, $drug_{load}$ is the amount of drug loaded inside NSVs and d.f. is the dilution factor used during the analysis.

Details are reported in the Supplementary data.

Fig. 2. Physical stability analysis of NSVs@DOX and RPAR-NSVs@DOX. (A) Variation of backscattered (ΔBS%), (B) variation of transmitted (ΔT%) and (C) turbiscan stability index (TSI) were obtained as a function of incubation time (0–60 min) and sample height. (D) Mean diameter evaluation by DLS analysis as a function of storage time (0–28 days). All analysis has been performed at 25 °C and the resulting data is the average of three independent experiments.

2.2.5. Stability of NSVs in fetal bovine serum (FBS) and human plasma
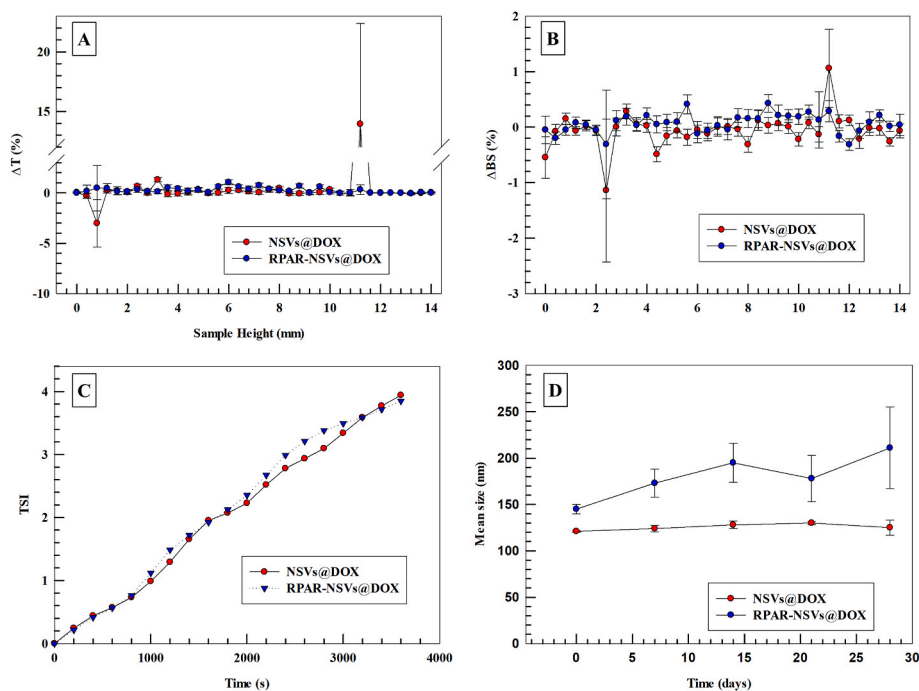
The physical stability of RPAR-NSVs@DOX in FBS and human plasma was evaluated as previously reported with some modifications [30].

Details of the stability studies in FBS and Human plasma are reported in the Supplementary data.

2.2.6. Uptake studies

The uptake studies of RPAR-NSVs in PPC-1 and M21 cells were evaluated using fluorescence confocal microscopy and flow cytometry. Before the uptake studies, the expression of NRP-1 in PPC-1 and M21 cells was evaluated by fluorescence confocal microscopy by staining the cells with anti-NRP-1 antibody and DAPI. Cells stained with the only secondary antibody was used as control.

Details are reported in the Supplementary data.

2.2.7. Cytotoxic studies

PPC-1, M21 and 22Rv1 cells were seeded in 96-well plate (5000 cells/well and 10,000 cells/well for PPC-1/M21 and 22Rv1, respectively) and attached overnight. The cells were then treated with free DOX, RPAR-NSVs@DOX and NSVs@DOX for 1 h at different drug concentrations (0.1, 0.5, 1, 5 and 10 μM), washed with PBS and fresh medium was added. Treated cells were grown for an additional 24 h.

The cell viability percentage was calculated using the following equation:

$$\text{Cell viability}(\%) = \frac{\text{Abs}_{\text{T}}}{\text{Abs}_{\text{C}}} \times 100 \qquad (3)$$

where the Abs_{T} is the absorbance of treated cells, while Abs_{c} is the absorbance of control cells (untreated).

Details of the cell viability percentages are reported in the Supplementary data.

2.2.8. Statistical analysis

Significant differences between results were analyzed using one-way analysis of variance (ANOVA) and then confirmed by Tukey's multiple comparison test. The analyses were carried out by using SigmaPlot v.12 and Excel (Office 2010, Microsoft, USA). The probabilities were set at three different significance levels: *p < 0.05; **p < 0.01 and ***p < 0.001.

3. Results and discussion

3.1. Physicochemical characterization of NSVs

The physicochemical properties of colloidal nanocarriers play a crucial role in their efficacy and features, requiring optimization during the early development stages [39]. We used dynamic light scattering (DLS) analysis to study the average size, size distribution (polydispersity index or PDI), and zeta potential of the NSVs.

The average size of empty NSVs and RPAR-NSVs was 121 ± 5 nm and 155 ± 8 nm, respectively (Fig. 1). The larger size of RPAR-NSVs is likely due to the surface conjugation of the RPAR peptide, which creates an additional aqueous layer on the surface of NSVs [35]. The presence of the RPAR peptide on the surface of NSVs also led to an increase in their zeta potential, from -47.0 ± 3.5 (NSVs) to -37.0 ± 2 (RPAR-NSVs) (Fig. 1). This increase in zeta potential is attributed to the presence of arginine (R), resulting in an overall less negative surface charge. Furthermore, both NSVs and RPAR-NSVs showed similar PDI values, indicating a narrow size distribution of the nanocarriers [35].

These results provide the proof for the development of peptide and NSV nanocarriers with suitable physicochemical properties to enable effective delivery.

The average size of RPAR-NSVs@DOX (164 ± 4 nm) was similar to that of empty RPAR-NSVs (155 ± 8 nm) with a slight but non-significant increase of 9 nm, likely due to the presence of crystallized DOX in the aqueous core [40] (Table S1). A similar trend was observed for non-targeted DOX-loaded NSVs (NSVs@DOX) that showed a slight increase of average size following the loading of DOX (121 ± 5 nm for NSVs, and 128 ± 7 nm for NSVs@DOX). The zeta potentials of RPAR-NSVs@DOX and NSVs@DOX were like those of RPAR-NSVs and NSVs. The DOX loading did not change significantly the PDI (below 0.2)

of RPAR-NSVs and NSVs nanocarriers, which remained stable and did not aggregate during the drug loading (Table S1).

These results indicate that nanovesicles loaded with DOX, either with or without RPAR functionalization, may be suitable for use in anticancer therapy. The low PDI value indicated a narrow size distribution of NSVs, which is necessary for uniform and reproducible release of payloads over time [41]. Moreover, the net negative surface charge of NSVs suggested their physical stability due to the electrostatic repulsion among particles, which is crucial for their storage.

DLS data agreed TEM results. Indeed, the photograms collected from TEM analysis showed that the nanoparticles have a spherical shape and the conjugation of RPAR on the surface of NSVs increased the average size of nanoparticles. This effect depends on the increase of hydrodynamic diameter of the NSVs due to the presence of RPAR peptide on their surface. Moreover, the average diameter of NSVs analyzed by using TEM are in the range from 150 to 200 nm for the different tested samples and these results are like those obtained after DLS analysis (Fig. 1). The presence of darker spots in TEM images depended on the presence of salts, in particular Cl, Na, S, accumulated in some areas of the samples due to the buffer solution that has been used to hydrate the nanoparticles during the preparation procedure as reported in the relative materials and methods section (*2.2.1. Synthesis of RPAR-NSVs and DOX encapsulation*). All the analyzed nanocarriers had a round-like shape and an homogeneous distribution.

The surface of NSVs was functionalized with RPAR peptide by making a thioether bond between the thiol group of the cysteine in the N-terminal sequence of RPAR peptide (Cys-RPAR) and the maleimide group of DSPE-PEG2000-maleimide present on the external surface of NSVs bilayer. The RPAR conjugation was evaluated by measuring the fluorescence of the FAM-peptide using an external calibration curve. The results showed a conjugation efficiency of ~83%. The RPAR conjugation was selective and pH-dependent, which prevented potential interferences and/or cross-reactions between the peptide and the maleimide group of nanocarriers during synthesis, as previously reported for the conjugation of targeting molecules to the surface of other nanoparticles [42]. Qualitative evaluation of the conjugation of RPAR with DSPE-PEG2000-maleimide was carried out using NMR. The ^{1}H NMR spectra showed that the characteristic maleimide peaks at 6.7 ppm disappeared in the DSPE-PEG2000-mal-RPAR derivative (Fig. S1). This result is consistent with previous studies and indicates the absence of aromatic hydrogen groups in the lipid-peptide conjugate, confirming the proper sulfhydryl-maleimide reaction and the synthesis of a stable thioether bond [36].

The colloidal stability over time of resulting RPAR-NSVs@DOX was studied by using Turbiscan analysis and DLS investigation. The resulting data were further compared with NSVs@DOX (control) for each time point. Fig. 2 panel A and B showed that there are not significant differences between the RPAR-NSVs@DOX and NSVs@DOX; in fact, the kinetic profiles of both nanocarriers are similar and overlapped for the full scan of the analysis. RPAR-NSVs@DOX and NSVs@DOX had not any variations of backscattered (ΔBS%) and transmitted (ΔT%) light above $\pm$5%, thus demonstrating that nanocarriers are stable and any destabilization phenomena, such as flocculation, sedimentation and/or creaming, occurred during the analysis. Variations over the threshold of $\pm$5% obtained at samples height below or over 2 and 10 mm, respectively, are due to the presence of bubble air at the vial's bottom and air-liquid interfaces and are not related to destabilization processes [37]. This data was further confirmed by Turbiscan stability index (TSI) which showed that the kinetic profiles were overlapped for both samples with a similar trend obtained for other nanocarriers reported elsewhere (Fig. 2, Panel C) [43]. The data obtained by DLS analysis agreed Turbiscan Lab results and demonstrated that there was not significant modification of RPAR-NSVs@DOX and NSVs@DOX average diameter up to 4 weeks of storage at +4 °C. A slight and no significant increase (up to ~200 nm) was obtained for RPAR-NSVs@DOX after 4 weeks. Indeed, this size increase was always correlated to a proportional increase net of SD, thus
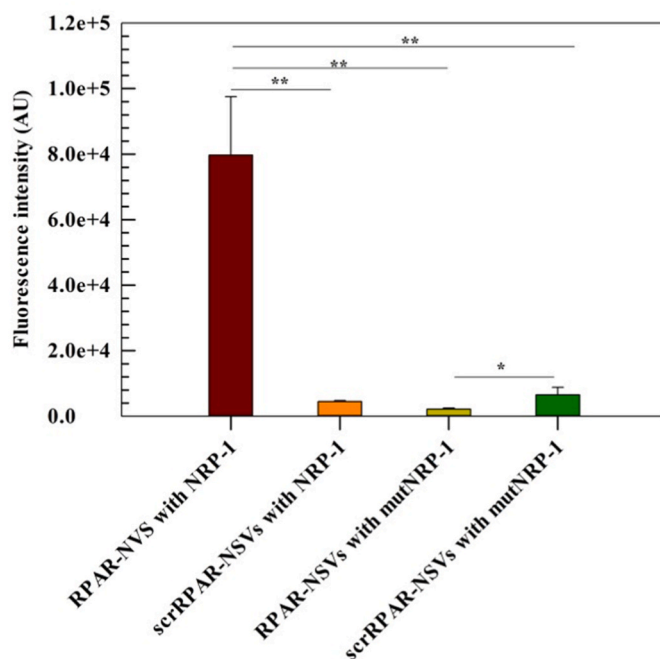
Fig. 3. Cell-free binding assay. Fluorescence-based cell-free binding assay was performed to evaluate the interaction between RPAR- or scrambled RPAR-functionalized nanovesicles (NSVs) with NRP-1 or mutNRP-1-coated beads. Following incubation, the released RPAR-NSVs or scrRPAR-NSVs were quantified using spectrofluorometer. The data represents the average of three independent experiments with standard deviation error bars. Statistical analysis showed significant differences between RPAR-NSVs and scrRPAR-NSVs incubated with NRP-1 coated beads, as well as between RPAR-NSVs and scrRPAR-NSVs incubated with mutNRP-1. *p < 0.05 and **p < 0.01 denote significant differences.

making these variations no significant. For this trend, we can speculate that the slight amount of DOX leaked by the lipid bilayer during the storage of nanocarriers at + 4 °C, interact with the peptide conjugated on the surface of RPAR-NSVs@DOX, thus resulting in an increased hydrophilicity of the surface with a consequent increase of water hydrodynamic layer surrounding the nanoparticle surface. However, the final average diameter of ~200 nm is still suitable for a potential systemic administration and does not affect the potential *in vivo* stability and injection of nanocarriers [44].

3.2. Cell-free binding study

We next tested the ability of RPAR-functionalized NSVs to interact with recombinant NRP-1 under cell-free conditions [38]. In control experiments, the mutant NRP-1 b1b2 domain with an inactive CendR binding pocket (mutNRP-1) and scrRPAR-NSVs were used. After incubation, RPAR-NSVs and scrRPAR-NSVs were released from the immobilized NRP-1 (or mutNRP-1) and quantified using FAM fluorimetry.

Our findings indicated that RPAR-NSVs exhibited a significantly higher binding to NRP-1 coated beads when compared to scrRPAR-NSVs (Fig. 3). Conversely, we observed negligible fluorescent signals after incubating RPAR-NSVs with mutNRP-1-coated beads. These results suggest that RPAR on the surface of NSVs is biologically active and capable of interacting with the CendR-binding pocket on the b1 domain of NRP-1 [45]. In addition, scrRPAR-NSVs displayed a modest binding affinity to mutNRP-1 (Fig. 3), which is likely attributable to non-specific interactions between scrRPAR-NSVs and mutNRP-1 under the tested conditions. The interaction between RPAR and NRP-1 is primarily based on a key-to-lock interaction between the peptidic ligand and the binding pocket of the receptor. Prototypical NRP-1 ligands VEGFA165,
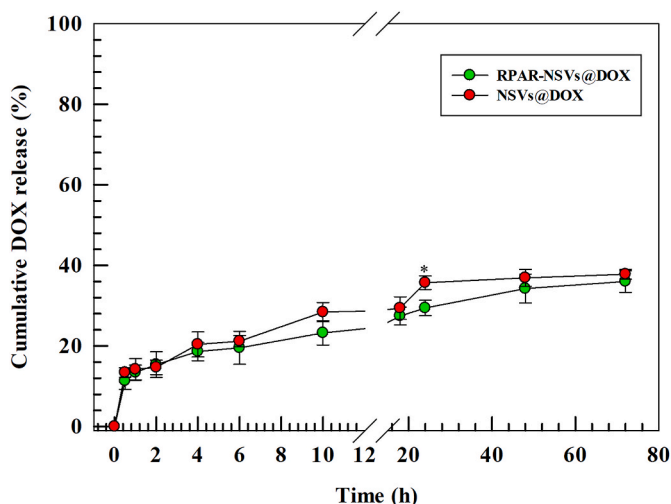
Fig. 4. DOX kinetic release profile. Drug release kinetic profiles were calculated using external calibration curves reported in the materials and methods section. The results are the average of three independent experiments ± standard deviation.

Semaphorin-3A and synthetic CendR peptides, use their C-terminal arginine residues to interact with the interloop cleft formed by the L3 loop (also termed "C-wall") and the L5 loop in the b1 domain of NRP-1 [45–47]. This interaction is highly dependent on the spatial orientation of amino acids involved in the binding interaction, and in the case of scrambled RPAR, the critical element for the activity of CendR peptides, the C-terminal arginine, is absent.

3.3. Entrapment efficiency and in vitro kinetic release of DOX

The entrapment efficiency (E.E.%) of DOX within RPAR-NSVs was 40.5 ± 2.6%, which falls within the range of previously reported values for similar NSV formulations [30]. Similar loading was observed for non-targeted NSVs@DOX, with a drug entrapment efficiency of 44.2 ± 1.7% (Table S1).

The high E.E.% was attributed to the crystallization of DOX in the aqueous core of NSVs. The crystallized drug was formed using the remote loading and pH gradient method, which is similar to the DOX encapsulation method used for the synthesis of Doxil®/Caelyx® liposomes [48]. Ammonium sulfate in the aqueous core of NSVs creates a transmembrane pH gradient, which allows the accumulation of DOX inside NSVs followed by precipitation of DOX-sulfate complex [49,50]. The E.E.% of DOX loaded inside NSVs (~40%) was lower than that achievable inside liposomes (>90%) [51,52]. This difference is attributed to the chemical structure and properties of the surfactants that are used for the synthesis of NSVs compared to lipids that are used for liposomes. In fact, surfactants in NSV bilayer have a single acyl chain compared to phospholipids which have double acyl chains and are more stable with a less permeable bilayer than NSVs. These results are consistent with data we have previously reported for similar NSVs [30].

The release kinetics of DOX from RPAR-NSVs was evaluated in Hepes buffer (pH 7.4). The release profile demonstrated a biphasic pattern, with an initial burst release observed during the first 2 h of incubation followed by a pseudo-steady state release with a cumulative release of 36 ± 2.7% after 72 h of incubation (Fig. 4). This release profile is consistent with previous reports for other nanocarriers that employ a combination of pH gradient and remote loading methods for entrapping DOX within the aqueous core [35]. The initial burst release may be attributed to the drug desorption from the surface of the NSVs or the leakage of DOX through the NSV bilayer, as previously reported [30]. DOX encapsulation in NSVs could potentially reduce its side effects, particularly cardiotoxicity, in healthy tissues, and thus increase the anticancer efficacy in tumor tissue after active targeting and passive accumulation by the extravasation through the irregular and fenestrated vasculature of tumor vessels [53]. Moreover, DOX release is not affected by the presence of RPAR peptide on the surface of NSVs as showed by the almost overlapped kinetic release profiles (Fig. 4).

3.4. Stability of NSVs in serum and human plasma

When nanocarriers come into contact with biological fluids, plasma proteins can adsorb onto their surface, creating a protein corona that alters the *in vivo* properties of nanoparticles, including biodistribution, pharmacokinetics, and stability [54–58]. The composition of this corona depends on the size, composition, and surface properties of the nanoparticles, which can be optimized to control the adsorption process. To evaluate the physicochemical properties of RPAR-NSVs@DOX, we incubated them with 10% (v/v) FBS and 50% (v/v) human plasma for 72 h, mimicking the *in vitro* and *in vivo* conditions of cell culture media and biological fluids, respectively (Fig. 5). Incubation in Hepes buffer was used as a negative control during the experiments. The incubation of NSVs with FBS did not cause significant shifts in the size of NSVs for up to 48 h of incubation, whereas the size doubled (415 ± 12 nm) by 72 h of incubation (Fig. 5). Probably, the huge increase of nanovesicle average size after 72 h of incubation depended on static condition of the experiments which, for long-incubation time, favored the formation of protein clusters that can induce the aggregation of nanocarriers [59–61]. Incubation of NSVs with human plasma led to a significant time-dependent change in the size. At early time points, the size of NSVs incubated with human plasma decreased (Fig. 5 B), while extending the incubation time to 72 h resulted in doubling of particle size (Fig. 5). The
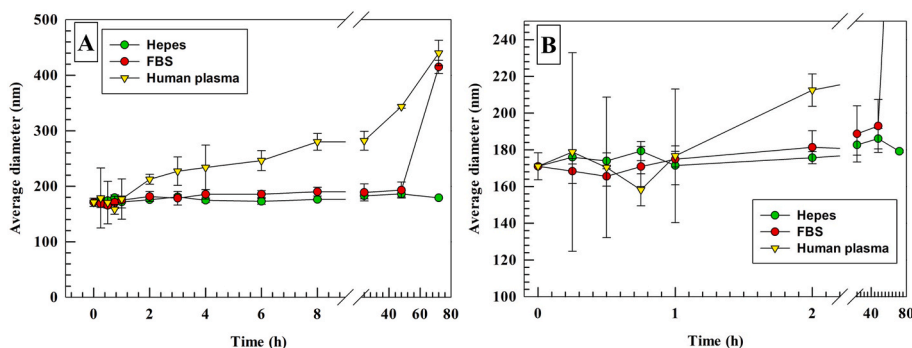
Fig. 5. Stability of RPAR-NSV@DOX in buffer and serum. The stability of RPAR-NSV@DOX was assessed by measuring the modification of the average size in Hepes buffer, fetal bovine serum (FBS) (10% v/v), and human plasma (50% v/v) over a 72-h period. The average size was measured using dynamic light scattering (DLS) and the results are presented as the mean ± standard deviation (SD) of three independent experiments. Panel B is a zoom of the early incubation time points (0–2 h). Statistical analysis of the data is provided in Table S2 in the supplementary materials.

PPC-1 CELLS
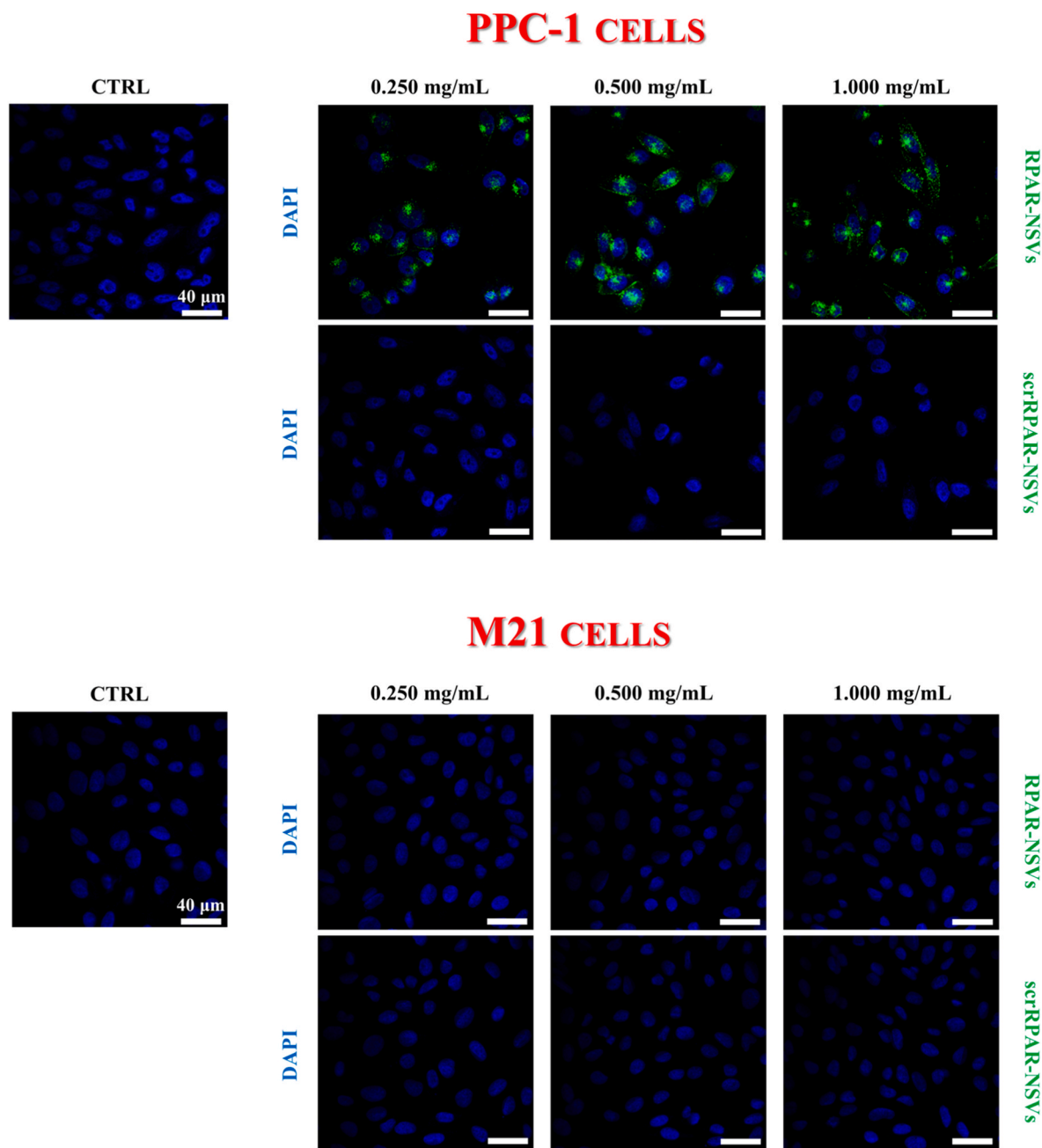
M21 CELLS

Fig. 6. Confocal laser scanning microscopy (CLSM) analysis demonstrates NRP-1-dependent intracellular uptake of RPAR-NSVs. PPC-1 and M21 cells were incubated with RPAR-NSVs or scrRPAR-NSVs for 1 h, at three different lipid concentrations (0.250, 0.500, and 1.000 mg/mL). The FAM fluorescence was detected through Alexa Fluor 488 (green) channel, while the nuclei were stained with DAPI (blue). Representative images show the intracellular uptake of RPAR-NSVs by PPC-1 cells, but not by NRP-1 negative M21 cells. Scale bar = 40 μm. The data shown are representative of three independent experiments. (For interpretation of the references to colour in this figure legend, the reader is referred to the Web version of this article.)

difference in the size of NSVs incubated in FBS and human plasma may be attributed to differences in protein composition and abundance between the two media [62]. The observed results can be explained by two stages that occur during the adsorption of the protein corona on the surface of the nanocarriers. Firstly, abundant proteins quickly adsorb onto the surface of the nanocarriers to form a soft corona composed of weakly interacting proteins [63,64]. The soft corona creates an osmotic pressure on the surface of the nanocarriers, leading to the shrinkage of the particles, which can be detected after the detachment of low-adsorbed proteins during the DLS analysis [65]. Secondly, low-abundance proteins with higher binding affinity for the surface of the nanocarriers replace the soft corona and form, a few hours after

interaction with serum/plasma components, the hard corona. These proteins are strongly adsorbed on the surface of the nanocarriers and cannot be easily detached [66].

After 2 h of incubation in human plasma, the average size of RPAR-NSVs@DOX showed a slow but continuous increase for up to 8 h (~80 nm). On the other hand, the increase in average size nearly doubled (440 ± 23 nm) after 72 h of incubation (Fig. 5).

Interestingly, the presence of polyethylene oxide (PEO) in the Tw20 backbone structure, which has pharmaceutical properties similar to those of polyethylene glycol (PEG) in PEGylated nanocarriers, maintained stable NSVs after interaction with biological components during the early stages of incubation [58]. However, the replacement of soft
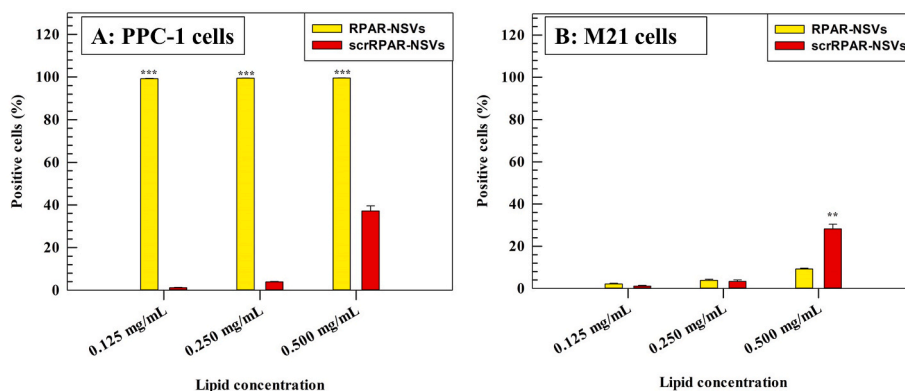
Fig. 7. Cellular internalization of RPAR-NSVs. PPC-1 (A) and M21 (B) cells were incubated with RPAR-NSVs or scrRPAR-NSVs for 1 h, and the uptake was quantified by flow cytometry. The results are shown as the percentage of fluorescent-positive cells as a function of nanovesicles concentration. At least 10,000 events were recorded for each analysis. The data presented are the average of three independent experiments ±standard deviation. The statistical significance of the differences between RPAR-NSVs and scrRPAR-NSVs was determined using Anova test: $*p < 0.05$, $**p < 0.01$, and $***p < 0.001$. FACS histogram shift are reported in the supplementary materials (Fig. S3).

corona with hard corona many hours after interaction with human plasma caused the detachment of part of PEO from the surface of NSVs, similar to the case of PEG from PEGylated liposomes [40]. This detachment modified the stability of nanocarriers, resulting in a significant increase in the average size. The static conditions of the study may have further enhanced this effect.

3.5. Cellular uptake studies

The intracellular uptake of RPAR-NSVs was evaluated using two different techniques, confocal laser scanning microscopy (CLSM) and flow cytometry, in two different cell lines. PPC-1 cells overexpress the NRP-1 receptor while M21 does not express this receptor, as showed by fluorescence confocal microscopy analysis. Indeed, PPC-1 cells showed a high fluorescent signal of NRP-1 protein (green) after the staining of cells with green-dye anti-NRP-1 antibody, whereas M21 cells lack the fluorescent signal showing the expression of NRP-1 (Fig. S2). The purpose was to investigate the targeting-mediated intracellular uptake of RPAR-NSVs via the NRP-1 receptor. scrRPAR-NSVs were used as a negative control. The CLSM analysis was performed at three different lipid concentrations (0.250, 0.500, and 1.000 mg/mL), with RPAR-NSVs and scrRPAR-NSVs incubated with the cells for 1 h (Fig. 6). The intracellular fluorescent signal increased as the concentration of RPAR-NSVs increased, although no significant differences were observed when comparing 0.500 and 1.000 mg/mL RPAR-NSV concentrations (Fig. 6), suggesting potential saturation of NRP-1 receptors during the incubation. In contrast, no fluorescence signal was obtained when treating PPC-1 cells with scrRPAR-NSVs, further demonstrating the essential role of the CendR motif of RPAR peptide in efficiently targeting the NRP-1 receptor overexpressed in this cell line (Fig. 6). Similarly, no significant uptake was observed in NRP-1-negative M21 cells treated with either RPAR-NSVs or scrRPAR-NSVs (Fig. 6).

CLSM analysis was complemented by flow cytometry to quantitatively test the targeting capability of RPAR-NSVs (Fig. 7 and Fig. S3). Due to its higher sensitivity, flow cytometry was conducted using a lower NSV concentration than that used for CLSM. RPAR-NSVs were robustly internalized in NRP-1-positive PPC-1 cells (Fig. 7A), consistent with the CLSM analysis (Fig. 6). FAM-labelled RPAR-NSVs were found to be taken up by nearly 100% of PPC-1 cells at tested concentrations (0.125–0.500 mg/mL). In contrast, less than 10% of PPC-1 cells incubated with scrRPAR-NSVs at lipid concentrations ranging between 0.125 and 0.250 mg/mL were fluorescent, and this increased to only ~40% at a concentration of 0.500 mg/mL (Fig. 7A). These differences demonstrate that the uptake of RPAR-NSVs in PPC-1 cells is receptor-specific. On the other hand, M21 cells showed similar intracellular uptake of
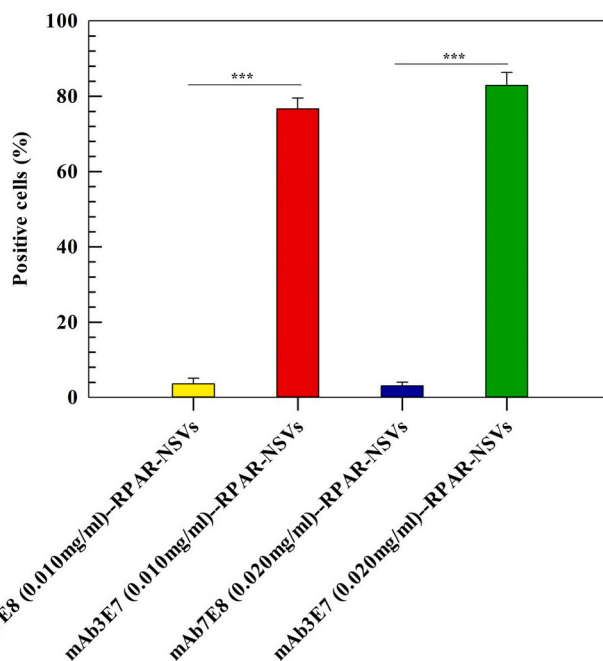
Fig. 8. NRP-1 CendR-binding pocket-dependent uptake of RPAR-NSVs by PPC-1 cells. The internalization of RPAR-NSVs was assessed in PPC-1 cells pre-incubated with either NRP-1 CendR-binding pocket-blocking (mAb7E8) or non-blocking (mAb7E7) antibodies. Following 2 h of incubation with the antibodies, the cells were exposed to RPAR-NSVs for an additional hour. The uptake of nanocarriers was quantified by flow cytometry, with at least 10,000 events recorded for each measurement. The results, presented as the percentage of FAM fluorescence-positive cells, demonstrate that the intracellular uptake of RPAR-NSVs in PPC-1 cells was significantly reduced in the presence of blocking mAb7E8 (0.01 and 0.02 mg/mL), compared to non-blocking mAb7E7 at the same concentrations. The data represents the average of three independent experiments ±standard deviation. Statistical significance was set at $***p < 0.001$.

both RPAR-NSVs and scrRPAR-NSVs, expect for the highest lipid concentration (Fig. 7B).

To further investigate the NRP-1 mediated uptake of RPAR-NSVs, PPC-1 cells were pre-incubated with NRP-1 b1 domain-binding monoclonal antibodies that are CendR binding pocket blocking (mAb7E8) or non-blocking (mAB3E7) [67]. When the cells were pre-incubated with CendR-blocking mAb7E8 at 0.01 and 0.02 mg/mL, the intracellular
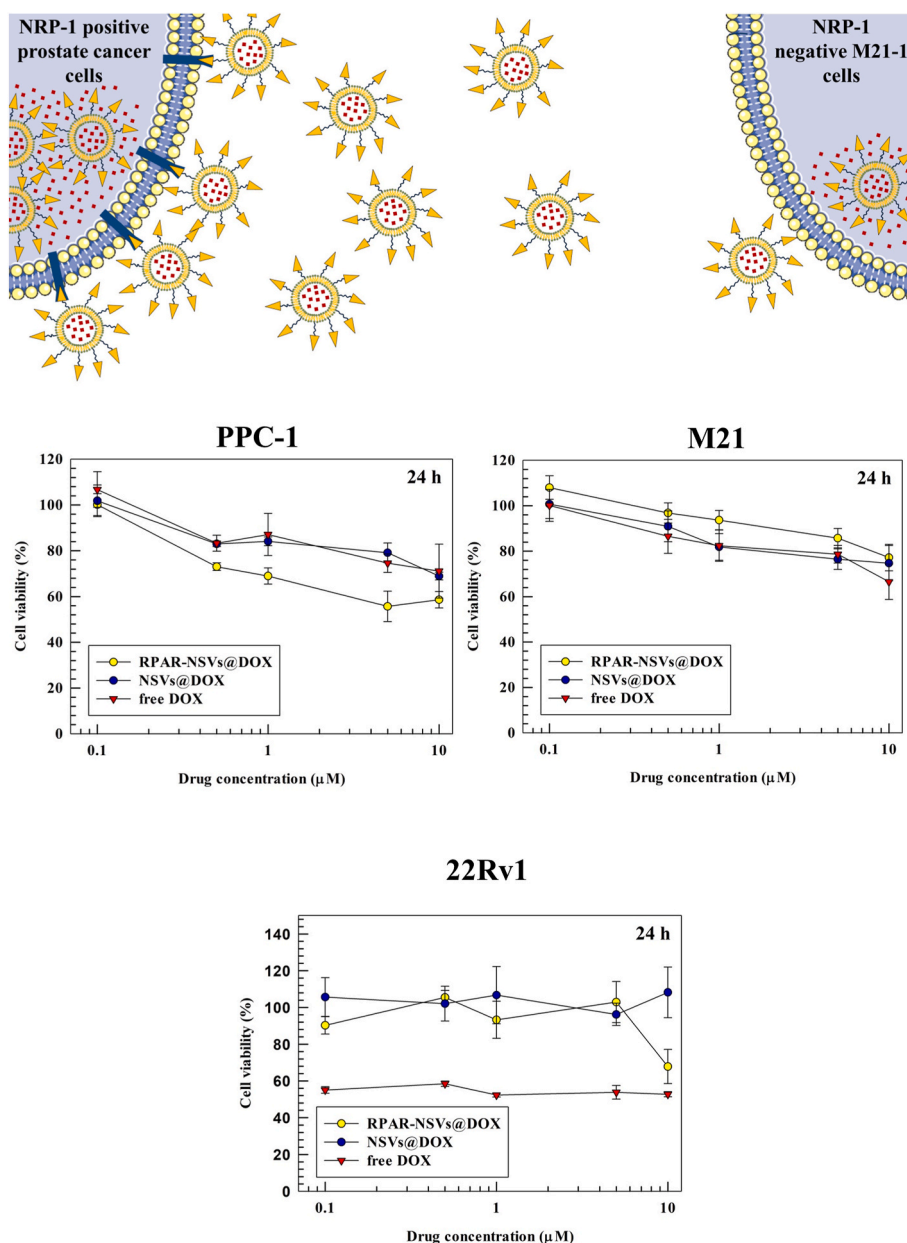
Fig. 9. *In vitro* effects of NSVs on the viability of PPC-1, 22Rv1 and M21 cells. The upper panel illustrates the schematic representation of RPAR-NSV@DOX uptake and intracellular DOX release, with NRP-1 receptor-mediated uptake observed only in PPC-1 cells. The cytotoxicity of RPAR-NSVs@DOX, NSVs@DOX, and free DOX treatment (1 h) was tested at different concentrations of DOX (0.1, 0.5, 1, 5, and 10 μM). After incubation, cells were grown in fresh medium for an additional 24 h. Untreated cells were used as negative controls and represented 100% cell viability. Empty nanocarriers (both functionalized and not) were tested showing the absence of cytotoxic effect on tested cell lines (data not shown). The results represent the average of three independent experiments ± standard deviation. Further statistical analysis of the data is available in the supplementary materials (Table S3).

uptake of RPAR-NSVs in NRP-1 positive PPC-1 cells was less than 10% (Fig. 8). In contrast, when the same concentrations of non-blocking mAB3E7 antibody were used for pre-incubation, approximately 80% of treated cells showed positive internalization of RPAR-NSVs (Fig. 8). These results agree with CLSM (Fig. 6) and flow cytometry (Fig. 7) data and demonstrate the selectivity of RPAR-NSVs towards NRP-1 and the related uptake in cancer cells overexpressing the NRP-1 receptor on their surface.

3.6. In vitro anticancer effect of NSVs

We next evaluated the effects of DOX-loaded RPAR-NSVs (RPAR-NSVs@DOX), free DOX, and non-functionalized DOX-loaded NSVs (NSVs@DOX) on the viability of PPC-1, M21 and 22Rv1 cells. The cells were treated with DOX loaded-NSVs or free DOX at 0.1, 0.5, 1, 5, and 10 μM drug concentration and incubated for 1 h. Afterwards, cells were washed with PBS and incubated for another 24 h before the evaluation of cytotoxic effect of different formulations (Fig. 9). For free DOX, a slight decrease in cell viability was observed in PPC-1 cells compared to M21 cells but this difference was not statistically significant (Fig. 9). NSVs@DOX had a similar effect on cell viability as free DOX in PPC-1 and M21 cells (Fig. 9). However, RPAR-NSVs@DOX significantly decreased cell viability of PPC-1 cells in a dose-dependent manner, with the cell viability <70% at 1 μM DOX and decreasing to ~55% at 5 μM DOX (Fig. 9 and Table S3). The effect of RPAR-NSVs@DOX plateaued at higher concentrations, suggesting saturation of the CendR binding sites (Fig. 9). We also showed that non-targeted DOX-NSVs have a minimal effect on 22Rv1, with a cell viability that consistently remains at

approximately 90% for all the tested concentrations. Our results demonstrate that at 10 μM concentration of DOX and RPAR-DOX-NSVs are significantly (**) more potent than non-targeted DOX-NSVs in NRP-1 positive 22Rv1 [68], which further supports the broader applicability of specific peptide-mediated drug delivery. Conversely to PPC-1 cells, in 22Rv1 cell line free DOX showed a higher cytotoxic effect compared to RPAR-DOX-NSVs and DOX-NSVs. This effect by using 2D *in vitro* models may depend on the both the higher sensitivity for DOX of 22Rv1 cells than PPC-1 cells, and the crystallized form of DOX inside the core of the nanovesicles that may cause a slow release of drug after nanocarrier intracellular uptake, thus leading to a depot-like system into the cells that is suitable for sustained release of DOX and extended effect by using *in vivo* models [48]. This effect can provide an improved efficacy of DOX anticancer effect *in vivo*. In fact, the higher cytotoxic effect of free DOX *in vitro* in monolayer cell culture models is not significantly predictable of its anticancer activity by using *in vivo* models because the free drugs are distributed in the bloodstream, quickly metabolized and eliminated by clearance organs [69].

RPAR-NSVs@DOX can decrease the quick metabolism and clearance of drug after *in vivo* injection, due to the crystallized DOX in their aqueous core and their slow release, and thus promoting the massive nanoparticle accumulation in the prostate cancer cells due to the over-expression of NRP-1 receptor.

In M21 cells, no significant differences in cell viability between RPAR-NSVs@DOX, NSVs@DOX, and free DOX were observed at 0.1, 0.5, and 10 μM equivalent DOX concentrations. However, at 1 and 5 μM, RPAR-NSVs@DOX showed lower cytotoxicity than NSVs@DOX and free DOX. The higher cytotoxic effect of NSVs@DOX than RPAR-NSVs@DOX in NRP-1 negative M21 cells can be attributed to the lower uptake of RPAR-NSVs@DOX than NSVs@DOX, probably due to the high hydrophilic properties of the surface in RPAR-NSVs compared to NSVs, causing non-specific binding.

4. Conclusions

RPAR-NSVs have suitable physicochemical properties for *in vitro* application and provide a proof of concept for the potential *in vivo* use of CendR peptides-conjugated to niosomes to have a selective targeting in prostate cancer. RPAR-NSVs are stable in artificial biological fluids mimicking the bloodstream. They specifically target NRP-1 receptors overexpressed in solid tumors, and their interaction with the neutrophil in receptors depends on the conjugated RPAR peptide. The conjugation of RPAR peptide on the surface of NSVs significantly improved the uptake rate in PPC-1 cells (RPAR-NSVs were taken up ca.10 times than NSVs), while no-significant differences were obtained in M21 cells. The NRP-1 mediated uptake process of RPAR-NSVs was further confirmed by using NRP-1 CendR-binding pocket-blocking (mAb7E8) antibody that blocked the internalization rate of RPAR-NSVs in PCC-1 NRP-1 positive cells from ~80% to 3%. DOX are loaded into RPAR-NSVs by using pH gradient and remote loading procedures, and the release of the drug from NSVs is biphasic. RPAR-NSVs@DOX decrease the cell viability of PCC-1 and 22Rv-1 cells in a dose- and time-dependent manner, while M21 cells, that does not over-express the NRP-1 receptors, show no significant differences for cell viability between RPAR-NSVs@DOX, NSVs@DOX. Our results highlight the potential use of CendR peptide-guided NSVs for the selective treatment of prostate cancer as well as other solid tumors over-expressing NRP-1 receptor. In particular, the proof of concept provided in this study by prototypic CendR peptide RPARPAR-functionalized NSVs lay the foundations for further *in vivo* studies by using more complex targeting peptides, such as iRGD or other CendR peptides, that also target the primary recruitment receptors (e.g. integrins) and are then proteolytically activated into CendR peptides in the tumor microenvironment.

CRediT author statement

Nicola d'Avanzo (N.d'A.): Data curation, Investigation, Formal analysis, and Writing/Revising and Editing – original draft; Valeria Sidorenko (V.S.): Investigation, Data curation, Formal analysis, Writing/Revising and Editing – original draft; Lorena Simón-Gracia (L.S-G.): Data curation, Investigation, Formal analysis, and Writing/Revising – original draft; Antonella Rocchi (A.R.): Data curation, Investigation; Ilaria Ottonelli (I.O.): Data curation, Investigation; Barbara Ruozi (B.R.): Data curation; Francesca Longo (F.L.): Data curation, Investigation; Christian Celia (C.C.): Writing/Revising – original draft, Data curation, Conceptualization and Funding acquisition; Tambet Teesalu (T.T.): Writing/Revising – original draft, Data curation, Conceptualization and Funding acquisition.

Declaration of competing interest

The authors declare that they have no known competing financial interests or personal relationships that could have appeared to influence the work reported in this paper.

Data availability

Data will be made available on request.

Acknowledgement

Appendix A. Supplementary data

Supplementary data to this article can be found online at https://doi.org/10.1016/j.jddst.2023.105162.

References

[1] H. Sung, J. Ferlay, R.L. Siegel, M. Laversanne, I. Soerjomataram, A. Jemal, F. Bray, Global cancer statistics 2020: GLOBOCAN estimates of incidence and mortality worldwide for 36 cancers in 185 countries, CA A Cancer J. Clin. 71 (2021) 209–249, https://doi.org/10.3322/caac.21660.

[2] L. Wang, B. Lu, M. He, Y. Wang, Z. Wang, L. Du, Prostate cancer incidence and mortality: global status and temporal trends in 89 countries from 2000 to 2019, Publ. Health Forum 10 (2022), 811044, https://doi.org/10.3389/fpubh.2022.811044.

[3] R.L. Wilson, D.R. Taaffe, R.U. Newton, N.H. Hart, P. Lyons-Wall, D.A. Galvão, Obesity and prostate cancer: a narrative review, Crit. Rev. Oncol.-Hematol. 169 (2022), 103543, https://doi.org/10.1016/j.critrevonc.2021.103543.

[4] S.J. Kim, M.U. Park, H.K. Chae, W. Nam, S.W. Kim, H. Yu, H.G. Kim, G.H. Kang, J. Y. Park, Overweight and obesity as risk factors for biochemical recurrence of prostate cancer after radical prostatectomy, Int. J. Clin. Oncol. (2022) 1–8, https://doi.org/10.1007/s10147-021-02058-9.

[5] G. Gandaglia, R. Leni, F. Bray, N. Fleshner, S.J. Freedland, A. Kibel, P. Stattin, H. Van Poppel, C. La Vecchia, Epidemiology and prevention of prostate cancer, Eur. Urol. Oncol. (2021), https://doi.org/10.1016/j.euo.2021.09.006.

[6] R. Nader, J. El Amm, J.B. Aragon-Ching, Role of chemotherapy in prostate cancer, Asian J. Androl. 20 (2018) 221, https://doi.org/10.4103/aja.aja_40_17.

[7] J. Zhao, C. Zhang, W. Wang, C. Li, X. Mu, K. Hu, Current progress of nanomedicine for prostate cancer diagnosis and treatment, Biomed. Pharmacother. 155 (2022), 113714, https://doi.org/10.1016/j.biopha.2022.113714.

[8] M. Norouzi, M. Amerian, M. Amerian, F. Atyabi, Clinical applications of nanomedicine in cancer therapy, Drug Discovery Today 25 (2020) 107–125, https://doi.org/10.1016/j.drudis.2019.09.017.

[9] A. Wicki, D. Witzigmann, V. Balasubramanian, J. Huwyler, Nanomedicine in cancer therapy: challenges, opportunities, and clinical applications, J. Contr. Release 200 (2015) 138–157, https://doi.org/10.1016/j.jconrel.2014.12.030.

[10] Z. Li, S. Tan, S. Li, Q. Shen, K. Wang, Cancer drug delivery in the nano era: an overview and perspectives, Oncol. Rep. 38 (2017) 611–624, https://doi.org/10.3892/or.2017.5718.

[11] V. Petrikaite, N. D'Avanzo, C. Celia, M. Fresta, Nanocarriers overcoming biological barriers induced by multidrug resistance of chemotherapeutics in 2D and 3D cancer models, Drug Resist. Updates (2023), 100956, https://doi.org/10.1016/j.drup.2023.100956.

[12] L. Zhang, Z. Lin, Y. Chen, D. Gao, P. Wang, Y. Lin, Y. Wang, F. Wang, Y. Han, H. Yuan, Co-delivery of Docetaxel and Resveratrol by liposomes synergistically boosts antitumor efficiency against prostate cancer, Eur. J. Pharmaceut. Sci. 174 (2022), 106199, https://doi.org/10.1016/j.ejps.2022.106199.

[13] A. Goswami, N. Patel, V. Bhatt, M. Raval, M. Kundariya, N. Sheth, Lycopene loaded polymeric nanoparticles for prostate cancer treatment: formulation, optimization using Box-behnken design and cytotoxicity studies, J. Drug Delivery Sci. Technol. 67 (2022), 102930, https://doi.org/10.1016/j.jddst.2021.102930.

[14] J. Quick, N. Dos Santos, M.H. Cheng, N. Chander, C.A. Brimacombe, J. Kulkarni, R. van der Meel, Y.Y.C. Tam, D. Witzigmann, P.R. Cullis, Lipid nanoparticles to silence androgen receptor variants for prostate cancer therapy, J. Contr. Release 349 (2022) 174–183, https://doi.org/10.1016/j.jconrel.2022.06.051.

[15] M. Ghaffari, S.M. Kalantar, M. Hemati, A. Dehghani Firoozabadi, A. Asri, A. Shams, S. Jafari Ghalekohneh, F. Haghiralsadat, Co-delivery of miRNA-15a and miRNA-16–1 using cationic PEGylated niosomes downregulates Bcl-2 and induces apoptosis in prostate cancer cells, Biotechnol. Lett. 43 (2021) 981–994, https://doi.org/10.1007/s10529-021-03085-2.

[16] H. Zare-Zardini, A. Alemi, A. Taheri-Kafrani, S.A. Hosseini, H. Soltaninejad, A. A. Hamidieh, M. Haghi Karamallah, M. Farrokhifar, M. Farrokhifar, Assessment of a new ginsenoside Rh2 nanoniosomal formulation for enhanced antitumor efficacy on prostate cancer: an in vitro study, Drug Des. Dev. Ther. (2020) 3315–3324, https://doi.org/10.2147/DDDT.S261027.

[17] B.A. Witika, K.E. Bassey, P.H. Demana, X. Siwe-Noundou, M.S. Poka, Current advances in specialised niosomal drug delivery: manufacture, characterization and drug delivery applications, Int. J. Mol. Sci. 23 (2022) 9668, https://doi.org/10.3390/ijms23179668.

[18] X. Ge, M. Wei, S. He, W.-E. Yuan, Advances of non-ionic surfactant vesicles (niosomes) and their application in drug delivery, Pharmaceutics 11 (2019) 55, https://doi.org/10.3390/pharmaceutics11020055.

[19] D.A. Seleci, M. Seleci, F. Stahl, T. Scheper, Tumor homing and penetrating peptide-conjugated niosomes as multi-drug carriers for tumor-targeted drug delivery, RSC Adv. 7 (2017) 33378–33384, https://doi.org/10.1039/C7RA05071B.

[20] M. Ferrari, Cancer nanotechnology: opportunities and challenges, Nat. Rev. Cancer 5 (2005) 161–171, https://doi.org/10.1038/nrc1566.

[21] L. Simón-Gracia, H. Hunt, T. Teesalu, Peritoneal carcinomatosis targeting with tumor homing peptides, Molecules 23 (2018) 1190, https://doi.org/10.3390/molecules23051190.

[22] H.-B. Pang, G.B. Braun, T. Friman, P. Aza-Blanc, M.E. Ruidiaz, K.N. Sugahara, T. Teesalu, E. Ruoslahti, An endocytosis pathway initiated through neuropilin-1 and regulated by nutrient availability, Nat. Commun. 5 (2014) 4904, https://doi.org/10.1038/ncomms5904.

[23] A. Dean, S. Gill, M. McGregor, V. Broadbridge, H.A. Järveläinen, T. Price, Dual αV-integrin and neuropilin-1 targeting peptide CEND-1 plus nab-paclitaxel and gemcitabine for the treatment of metastatic pancreatic ductal adenocarcinoma: a first-in-human, open-label, multicentre, phase 1 study, Lancet Gastroenterol. Hepatol. 7 (2022) 943–951, https://doi.org/10.1016/S2468-1253(22)00167-4.

[24] C. Springfeld, J.P. Neoptolemos, CEND-1: a game changer for pancreatic cancer chemotherapy? Lancet Gastroenterol. Hepatol. 7 (2022) 900–902, https://doi.org/10.1016/S2468-1253(22)00197-2.

[25] E. Ruoslahti, Tumor penetrating peptides for improved drug delivery, Adv. Drug Delivery Rev. 110 (2017) 3–12, https://doi.org/10.1016/j.addr.2016.03.008.

[26] G. Balistreri, Y. Yamauchi, T. Teesalu, A widespread viral entry mechanism: the C-end Rule motif–neuropilin receptor interaction, Proc. Natl. Acad. Sci. U.S.A. 118 (2021), e2112457118, https://doi.org/10.1073/pnas.2112457118.

[27] S.-D. Liu, L.-P. Zhong, J. He, Y.-X. Zhao, Targeting neuropilin-1 interactions is a promising anti-tumor strategy, Chin. Med. J. 134 (2021) 508–517, https://doi.org/10.1097/CM9.0000000000001200.

[28] A.M. Jubb, L.A. Strickland, S.D. Liu, J. Mak, M. Schmidt, H. Koeppen, Neuropilin-1 expression in cancer and development, J. Pathol. 226 (2012) 50–60, https://doi.org/10.1002/path.2989.

[29] L. Simón-Gracia, V. Sidorenko, A. Uustare, I. Ogibalov, A. Tasa, O. Tshubrik, T. Teesalu, Novel anthracycline utorubicin for cancer therapy, Angew. Chem. 133 (2021) 17155–17164, https://doi.org/10.1002/anie.202016421.

[30] M. Di Francesco, C. Celia, M.C. Cristiano, N. d'Avanzo, B. Ruozi, C. Mircioiu, D. Cosco, L. Di Marzio, M. Fresta, Doxorubicin hydrochloride-loaded nonionic

[31] surfactant vesicles to treat metastatic and non-metastatic breast cancer, ACS Omega 6 (2021) 2973–2989, https://doi.org/10.1021/acsomega.0c05350.

[31] J. Guan, H. Guo, T. Tang, Y. Wang, Y. Wei, P. Seth, Y. Li, S.M. Dehm, E. Ruoslahti, H.B. Pang, iRGD-liposomes enhance tumor delivery and therapeutic efficacy of antisense oligonucleotide drugs against primary prostate cancer and bone metastasis, Adv. Funct. Mater. 31 (2021), 2100478, https://doi.org/10.1002/adfm.202100478.

[32] L. Palmas, M. Aroffu, G.L. Petretto, E. Escribano-Ferrer, O. Díez-Sales, I. Usach, J.-E. Peris, F. Marongiu, M. Ghavam, S. Fais, Entrapment of Citrus limon var. pompia essential oil or pure citral in liposomes tailored as mouthwash for the treatment of oral cavity diseases, Pharmaceuticals 13 (2020) 216, https://doi.org/10.3390/ph13090216.

[33] M.J. Pauwels, J. Xie, A. Ceroi, S. Balusu, J. Castelein, E. Van Wonterghem, G. Van Imschoot, A. Ward, T.R. Menheniott, O. Gustafsson, Choroid plexus-derived extracellular vesicles exhibit brain targeting characteristics, Biomaterials 290 (2022), 121830, https://doi.org/10.1016/j.biomaterials.2022.121830.

[34] J.T. Duskey, I. Ottonelli, F. Da Ros, A. Vilella, M. Zoli, S. Kovachka, F. Spyrakis, M. A. Vandelli, G. Tosi, B. Ruozi, Novel peptide-conjugated nanomedicines for brain targeting: in vivo evidence, Nanomed. Nanotechnol. Biol. Med. 28 (2020), 102226, https://doi.org/10.1016/j.nano.2020.102226.

[35] N. d'Avanzo, G. Torrieri, P. Figueiredo, C. Celia, D. Paolino, A. Correia, K. Moslova, T. Teesalu, M. Fresta, H.A. Santos, LinTT1 peptide-functionalized liposomes for targeted breast cancer therapy, Int. J. Pharm. 597 (2021), 120346, https://doi.org/10.1016/j.ijpharm.2021.120346.

[36] X. Wang, N. Meng, S. Wang, Y. Zhang, L. Lu, R. Wang, H. Ruan, K. Jiang, H. Wang, D. Ran, Non-immunogenic, low-toxicity and effective glioma targeting MTI-31 liposomes, J. Contr. Release 316 (2019) 381–392, https://doi.org/10.1016/j.jconrel.2019.11.005.

[37] A. Barone, A.M. Zimbo, N. d'Avanzo, A.M. Tolomeo, S. Ruga, A. Cardamone, C. Celia, M. Scalise, D. Torella, M. La Deda, Thermoresponsive M1 macrophage-derived hybrid nanovesicles for improved in vivo tumor targeting, Drug Delivery Transl. Res. (2023) 1–15, https://doi.org/10.1007/s13346-023-01378-9.

[38] G. Torrieri, F. Fontana, P. Figueiredo, Z. Liu, M.P. Ferreira, V. Talman, J.P. Martins, M. Fusciello, K. Moslova, T. Teesalu, Dual-peptide functionalized acetalated dextran-based nanoparticles for sequential targeting of macrophages during myocardial infarction, Nanoscale 12 (2020) 2350–2358, https://doi.org/10.1039/C9NR09934D.

[39] W. Chen, J. Li, Y. Xing, X. Wang, H. Zhang, M. Xia, D. Wang, Dual-pH sensitive charge-reversal drug delivery system for highly precise and penetrative chemotherapy, Pharm. Res. 37 (2020) 1–13, https://doi.org/10.1007/s11095-020-02852-6.

[40] G. Pasut, D. Paolino, C. Celia, A. Mero, A.S. Joseph, J. Wolfram, D. Cosco, O. Schiavon, H. Shen, M. Fresta, Polyethylene glycol (PEG)-dendron phospholipids as innovative constructs for the preparation of super stealth liposomes for anticancer therapy, J. Contr. Release 199 (2015) 106–113, https://doi.org/10.1016/j.jconrel.2014.12.008.

[41] M. Danaei, M. Dehghankhold, S. Ataei, F. Hasanzadeh Davarani, R. Javanmard, A. Dokhani, S. Khorasani, M. Mozafari, Impact of particle size and polydispersity index on the clinical applications of lipidic nanocarrier systems, Pharmaceutics 10 (2018) 57, https://doi.org/10.3390/pharmaceutics10020057.

[42] A. Marques, P. Costa, S. Velho, M. Amaral, Functionalizing nanoparticles with cancer-targeting antibodies: a comparison of strategies, J. Contr. Release 320 (2020) 180–200, https://doi.org/10.1016/j.jconrel.2020.01.035.

[43] J. Ye, Y. Yang, J. Jin, M. Ji, Y. Gao, Y. Feng, H. Wang, X. Chen, Y. Liu, Targeted delivery of chlorogenic acid by mannosylated liposomes to effectively promote the polarization of TAMs for the treatment of glioblastoma, Bioact. Mater. 5 (2020) 694–708, https://doi.org/10.1016/j.bioactmat.2020.05.001.

[44] E. Blanco, H. Shen, M. Ferrari, Principles of nanoparticle design for overcoming biological barriers to drug delivery, Nat. Biotechnol. 33 (2015) 941–951, https://doi.org/10.1038/nbt.3330.

[45] D. Zanuy, R. Kotla, R. Nussinov, T. Teesalu, K.N. Sugahara, C. Alemán, N. Haspel, Sequence dependence of C-end rule peptides in binding and activation of neuropilin-1 receptor, J. Struct. Biol. 182 (2013) 78–86, https://doi.org/10.1016/j.jsb.2013.02.006.

[46] M.W. Parker, P. Xu, X. Li, C.W. Vander Kooi, Structural basis for selective vascular endothelial growth factor-A (VEGF-A) binding to neuropilin-1, J. Biol. Chem. 287 (2012) 11082–11089, https://doi.org/10.1074/jbc.M111.331140.

[47] A. Antipenko, J.-P. Himanen, K. Van Leyen, V. Nardi-Dei, J. Lesniak, W.A. Barton, K.R. Rajashankar, M. Lu, C. Hoemme, A.W. Püschel, Structure of the semaphorin-3A receptor binding module, Neuron 39 (2003) 589–598, https://doi.org/10.1016/j.pbiomolbio.2015.03.006.

[48] Y.C. Barenholz, Doxil®—the first FDA-approved nano-drug: lessons learned, J. Contr. Release 160 (2012) 117–134, https://doi.org/10.1016/j.jconrel.2012.03.020.

[49] A. Fritze, F. Hens, A. Kimpfler, R. Schubert, R. Peschka-Süss, Remote loading of doxorubicin into liposomes driven by a transmembrane phosphate gradient, Biochim. Biophys. Acta 1758 (2006) 1633–1640, https://doi.org/10.1016/j.bbamem.2006.05.028.

[50] C.C. Cheung, W.T. Al-Jamal, Sterically stabilized liposomes production using staggered herringbone micromixer: effect of lipid composition and PEG-lipid content, Int. J. Pharm. 566 (2019) 687–696, https://doi.org/10.1016/j.ijpharm.2019.06.033.

[51] D. Liu, K. Li, L. Gong, L. Fu, D. Yang, Charge reversal Yolk-shell liposome Co-loaded JQ1 and doxorubicin with high drug loading and optimal ratio for synergistically enhanced tumor chemo-immunotherapy via blockade PD-L1

pathway, Int. J. Pharm. (2023), 122728, https://doi.org/10.1016/j.ijpharm.2023.122728.

[52] J.A. Duarte, E.R. Gomes, A.L.B. De Barros, E.A. Leite, Co-encapsulation of simvastatin and doxorubicin into pH-sensitive liposomes enhances antitumoral activity in breast cancer cell lines, Pharmaceutics 15 (2023) 369, https://doi.org/10.3390/pharmaceutics15020369.

[53] T. Shehata, Y. Kono, K. Higaki, T. Kimura, K.-i. Ogawara, In vivo distribution characteristics and anti-tumor effects of doxorubicin encapsulated in PEG-modified niosomes in solid tumor-bearing mice, J. Drug Delivery Sci. Technol. (2023), 104122, https://doi.org/10.1016/j.jddst.2022.104122.

[54] L. Landgraf, C. Christner, W. Storck, I. Schick, I. Krumbein, H. Dähring, K. Haedicke, K. Heinz-Herrmann, U. Teichgräber, J.R. Reichenbach, A plasma protein corona enhances the biocompatibility of Au@ Fe3O4 Janus particles, Biomaterials 68 (2015) 77–88, https://doi.org/10.1016/j.biomaterials.2015.07.049.

[55] M.C. Lo Giudice, L.M. Herda, E. Polo, K.A. Dawson, In situ characterization of nanoparticle biomolecular interactions in complex biological media by flow cytometry, Nat. Commun. 7 (2016), 13475, https://doi.org/10.1038/ncomms13475.

[56] M. Hadjidemetriou, Z. Al-Ahmady, M. Mazza, R.F. Collins, K. Dawson, K. Kostarelos, In vivo biomolecule corona around blood-circulating, clinically used and antibody-targeted lipid bilayer nanoscale vesicles, ACS Nano 9 (2015) 8142–8156, https://doi.org/10.1021/acsnano.5b03300.

[57] M. Hadjidemetriou, S. McAdam, G. Garner, C. Thackeray, D. Knight, D. Smith, Z. Al-Ahmady, M. Mazza, J. Rogan, A. Clamp, The human in vivo biomolecule corona onto PEGylated liposomes: a proof-of-concept clinical study, Adv. Mater. 31 (2019), 1803335, https://doi.org/10.1002/adma.201803335.

[58] E. Imperlini, C. Celia, A. Cevenini, A. Mandola, M. Raia, M. Fresta, S. Orrù, L. Di Marzio, F. Salvatore, Nano-bio interface between human plasma and niosomes with different formulations indicates protein corona patterns for nanoparticle cell targeting and uptake, Nanoscale 13 (2021) 5251–5269, https://doi.org/10.1039/D0NR07229J.

[59] D. Pozzi, G. Caracciolo, A.L. Capriotti, C. Cavaliere, G. La Barbera, T. J. Anchordoquy, A. Laganà, Surface chemistry and serum type both determine the nanoparticle–protein corona, J. Proteonomics 119 (2015) 209–217, https://doi.org/10.1016/j.jprot.2015.02.009.

[60] A.L. Barrán-Berdón, D. Pozzi, G. Caracciolo, A.L. Capriotti, G. Caruso, C. Cavaliere, A. Riccioli, S. Palchetti, A. Laganà, Time evolution of nanoparticle–protein corona in human plasma: relevance for targeted drug delivery, Langmuir 29 (2013) 6485–6494, https://doi.org/10.1021/la401192x.

[61] S. Palchetti, V. Colapicchioni, L. Digiacomo, G. Caracciolo, D. Pozzi, A.L. Capriotti, G. La Barbera, A. Laganà, The protein corona of circulating PEGylated liposomes, Biochim. Biophys. Acta, Biomembr. 1858 (2016) 189–196, https://doi.org/10.1016/j.bbamem.2015.11.012.

[62] T. Cedervall, I. Lynch, S. Lindman, T. Berggård, E. Thulin, H. Nilsson, K.A. Dawson, S. Linse, Understanding the nanoparticle–protein corona using methods to quantify exchange rates and affinities of proteins for nanoparticles, Proc. Natl. Acad. Sci. U. S.A. 104 (2007) 2050–2055, https://doi.org/10.1073/pnas.0608582104.

[63] A.M. Makarieva, V.G. Gorshkov, B.-L. Li, S.L. Chown, P.B. Reich, V.M. Gavrilov, Mean mass-specific metabolic rates are strikingly similar across life's major domains: evidence for life's metabolic optimum, Proc. Natl. Acad. Sci. U.S.A. 105 (2008) 16994–16999, https://doi.org/10.1073/pnas.0802148105.

[64] M.P. Monopoli, D. Walczyk, A. Campbell, G. Elia, I. Lynch, F. Baldelli Bombelli, K. A. Dawson, Physical− chemical aspects of protein corona: relevance to in vitro and in vivo biological impacts of nanoparticles, J. Am. Chem. Soc. 133 (2011) 2525–2534, https://doi.org/10.1021/ja107583h.

[65] J. Wolfram, K. Suri, Y. Yang, J. Shen, C. Celia, M. Fresta, Y. Zhao, H. Shen, M. Ferrari, Shrinkage of pegylated and non-pegylated liposomes in serum, Colloids Surf., B 114 (2014) 294–300, https://doi.org/10.1016/j.colsurfb.2013.10.009.

[66] J. Wolfram, Y. Yang, J. Shen, A. Moten, C. Chen, H. Shen, M. Ferrari, Y. Zhao, The nano-plasma interface: implications of the protein corona, Colloids Surf., B 124 (2014) 17–24, https://doi.org/10.1016/j.colsurfb.2014.02.035.

[67] J.L. Daly, B. Simonetti, K. Klein, K.-E. Chen, M.K. Williamson, C. Antón-Plágaro, D. K. Shoemark, L. Simón-Gracia, M. Bauer, R. Hollandi, Neuropilin-1 is a host factor for SARS-CoV-2 infection, Science 370 (2020) 861–865, https://doi.org/10.1126/science.abd3072.

[68] P. Zhang, L. Chen, F. Zhou, Z. He, G. Wang, Y. Luo, NRP1 promotes prostate cancer progression via modulating EGFR-dependent AKT pathway activation, Cell Death Dis. 14 (2023) 159, https://doi.org/10.1038/s41419-023-05696-1.

[69] E. Alphandéry, P. Grand-Dewyse, R. Lefèvre, C. Mandawala, M. Durand-Dubief, Cancer therapy using nanoformulated substances: scientific, regulatory and financial aspects, Expert Rev. Anticancer Ther. 15 (2015) 1233–1255, https://doi.org/10.1586/14737140.2015.1086647.